System-size and centrality dependence of charged kaon and pion production in nucleus-nucleus collisions at 40A GeV and 158A GeV beam energy

T. Anticic,[22] B. Baatar,[8] D. Barna,[4] J. Bartke,[6] H. Beck,[9] L. Betev,[10] H. Białkowska,[19] C. Blume,[9] M. Bogusz,[21] B. Boimska,[19] J. Book,[9] M. Botje,[1] P. Bunčić,[10] T. Cetner,[21] P. Christakoglou,[1] P. Chung,[18] O. Chvala,[14] J. G. Cramer,[18] P. Dinkelaker,[9] V. Eckardt,[13] Z. Fodor,[4] P. Foka,[7] V. Friese,[7] M. Gaździcki,[9,11] K. Grebieszkow,[21] C. Höhne,[7] K. Kadija,[22] A. Karev,[10] M. Kliemant,[9] V. I. Kolesnikov,[8] T. Kollegger,[9] M. Kowalski,[6] D. Kresan,[7] A. Laszlo,[4] R. Lacey,[18] M. van Leeuwen,[1] B. Lungwitz,[9] M. Mackowiak,[21] M. Makariev,[17] A. I. Malakhov,[8] M. Mateev,[16] G. L. Melkumov,[8] M. Mitrovski,[9] St. Mrówczyński,[11] V. Nicolic,[22] G. Pálla,[4] A. D. Panagiotou,[2] W. Peryt,[21] J. Pluta,[21] D. Prindle,[15] F. Pühlhofer,[12] R. Renfordt,[9] C. Roland,[5] G. Roland,[5] M. Rybczyński,[11] A. Rybicki,[6] A. Sandoval,[7] N. Schmitz,[13] T. Schuster,[9] P. Seyboth,[13] F. Siklér,[4] E. Skrzypczak,[20] M. Slodkowski,[21] G. Stefanek,[11] R. Stock,[9] H. Ströbele,[9] T. Susa,[22] M. Szuba,[21] M. Utvić,[9] D. Varga,[3] M. Vassiliou,[2] G. I. Veres,[4] G. Vesztergombi,[4] D. Vranić,[7] Z. Włodarczyk,[11] and A. Wojtaszek-Szwarc[11]

(NA49 Collaboration)

[1]*NIKHEF, Amsterdam, Netherlands*
[2]*Department of Physics, University of Athens, Athens, Greece*
[3]*Eötvös Loránt University, Budapest, Hungary*
[4]*Wigner Research Centre for Physics, Hungarian Academy of Sciences, Budapest, Hungary*
[5]*Massachusetts Institute of Technology, Cambridge, Massachusetts, USA*
[6]*H. Niewodniczański Institute of Nuclear Physics, Polish Academy of Sciences, Cracow, Poland*
[7]*GSI Helmholtzzentrum für Schwerionenforschung, Darmstadt, Germany*
[8]*Joint Institute for Nuclear Research, Dubna, Russia*
[9]*Fachbereich Physik der Universität, Frankfurt, Germany*
[10]*CERN, Geneva, Switzerland*
[11]*Institute of Physics, Jan Kochanowski University, Kielce, Poland*
[12]*Fachbereich Physik der Universität, Marburg, Germany*
[13]*Max-Planck-Institut für Physik, Munich, Germany*
[14]*Institute of Particle and Nuclear Physics, Charles University, Prague, Czech Republic*
[15]*Nuclear Physics Laboratory, University of Washington, Seattle, Washington, USA*
[16]*Atomic Physics Department, Sofia University St. Kliment Ohridski, Sofia, Bulgaria*
[17]*Institute for Nuclear Research and Nuclear Energy, BAS, Sofia, Bulgaria*
[18]*Department of Chemistry, Stony Brook University (SUNYSB), Stony Brook, New York, USA*
[19]*Institute for Nuclear Studies, Warsaw, Poland*
[20]*Institute for Experimental Physics, University of Warsaw, Warsaw, Poland*
[21]*Faculty of Physics, Warsaw University of Technology, Warsaw, Poland*
[22]*Rudjer Boskovic Institute, Zagreb, Croatia*

Measurements of charged pion and kaon production are presented in centrality selected Pb + Pb collisions at 40A GeV and 158A GeV beam energy as well as in semicentral C + C and Si + Si interactions at 40A GeV. Transverse mass spectra, rapidity spectra, and total yields are determined as a function of centrality. The system-size and centrality dependence of relative strangeness production in nucleus-nucleus collisions at 40A GeV and 158A GeV beam energy are derived from the data presented here and from published data for C + C and Si + Si collisions at 158A GeV beam energy. At both energies a steep increase with centrality is observed for small systems followed by a weak rise or even saturation for higher centralities. This behavior is compared to calculations using transport models (ultra-relativistic quantum molecular dynamics and hadron-string dynamics), a percolation model, and the core-corona approach.

I. INTRODUCTION

Strangeness production has always been an important observable for probing the state of matter created in heavy-ion collisions. The yields of the various strange hadrons, properly normalized to those in elementary nucleon-nucleon interactions, are expected to exhibit different behavior in partonic than in hadronic environments [1]. The number of created strange quark-antiquark pairs per participating nucleon is significantly higher in central Pb + Pb collisions than in $p + p$ interactions

at all collision energies. A maximum in the yield of the K^+ relative to that of the π^+ in central Pb + Pb collisions was observed by NA49 at about 30A GeV beam energy [2,3] and interpreted as evidence for the onset of deconfinement. Microscopic models such as hadron-string dynamics (HSD) and ultra-relativistic quantum molecular dynamics (UrQMD) do not predict a maximum. In the statistical model this structure can only be reproduced by including additional features like those introduced in [4], i.e., high mass resonances beyond the

ones listed in [5] and a significant contribution by σ meson states. There are no indications for a similar nonmonotonic energy dependence of this ratio in $p + p$ interactions. In order to better understand the observed maximum in the energy dependence observed in central Pb + Pb collisions, measurements of the system size dependence of strangeness production are needed for different strangeness carriers and at various energies.

NA49 has published data on the system-size dependence of hyperon (Λ and Ξ) [6] and (anti)proton yields and distributions [7] in Pb + Pb collisions at $40A$ GeV and $158A$ GeV beam energy. Results on pions, kaons, ϕ mesons, and Λ hyperons in C + C and Si + Si at $158A$ GeV were reported in Ref. [8]. Pion and kaon production was also studied in $p + p$ interactions at 158 GeV/c [9,10]. The present study completes these results by a measurement of the centrality dependence of pion and kaon production in Pb + Pb collisions at $40A$ GeV and $158A$ GeV beam energy as well as for C + C (66% most central) and Si + Si (29% most central) interactions at $40A$ GeV. These results provide a link between the centrality selected data on pion and kaon production at lower [GSI Heavy Ion Synchrotron (SIS) and Alternating Gradient Synchrotron (AGS)] and higher [Relativistic Heavy Ion Collider (RHIC)] energy. At SIS and AGS energies kaon and pion production was studied in centrality selected Au + Au collisions as well as in collisions of smaller systems such as Si + Al [11–13]. Here, a rather linear increase is observed for relative kaon production with the number of participants. On the other hand, at RHIC energies a clear saturation behavior is found for collisions with more than approximately 60 nucleons participating in the collision [14,15]. The same observation has also been made at top Super Proton Synchrotron (SPS) energies by comparing central C + C, Si + Si, and Pb + Pb collisions [8].

Statistical models based on the grand-canonical ensemble have been used to describe strange particle yields in central collisions of heavy nuclei at high energies [4,16,17]. For smaller reaction volumes, because of the lower number of produced strange quarks, restrictions due to strangeness conservation arise, which suppress strangeness production with respect to the infinite-volume limit. This is taken into account by using canonical ensembles in the statistical model calculations. The transition from the canonical to the grand-canonical ensemble would thus result in a characteristic volume dependence of strangeness production [18,19]. When comparing statistical model results to experimental data in terms of reaction volume, the latter has to be related to an experimental observable. In Refs. [19,20] the reaction volume was assumed to be proportional to the number of wounded nucleons (see Sec. III). However, with this approach the data at SPS energies and above could not be described satisfactorily [21]. Good agreement can be achieved if the relevant volume is subject to additional geometric constraints which restrict strangeness conservation to subvolumes, as realized for example in the percolation models. The corresponding calculations suggest that not only are several subvolumes formed for small systems but that also in central collisions not all nucleon-nucleon collisions are included in the central volume [21]. A simpler implementation of this ansatz is realized in the so-called core-corona model [22,23]. It is built on the assumption that the fireball created in nuclear collisions is composed of a core, which has the same properties as a very central collision system, and a corona, which is a superposition of independent nucleon-nucleon interactions. The sizes of core and corona can be defined by the condition that the corona is formed by those nucleon-nucleon collisions in which both partners interact only once during the whole collision process. The fraction of single scatterings is calculated using straight-line geometry as described in the Glauber model [24]. This approach was recently successfully applied to the system-size dependence of strangeness production at RHIC energies [25,26] and for the above-mentioned hyperon production at SPS [6]. The common features of such model calculations at fixed energy are a fast increase of relative strangeness production with system size for small reaction volumes (below approximately 60 participating nucleons) and eventual saturation for large system sizes.

II. THE NA49 EXPERIMENT

The NA49 detector is a large-acceptance hadron spectrometer at the CERN SPS [27]. The main components are four large time projection chambers (TPCs) and two superconducting dipole magnets with a one-meter vertical gap, aligned in a row, and a total bending power of 9 Tm. The magnetic field was set a factor of 4 lower for data taking at $40A$ GeV than at $158A$ GeV. Two two-meter-long TPCs (VTPCs) inside the magnets each with 72 pad rows along the beam direction allow for precise tracking, momentum determination, vertex reconstruction, and particle identification (PID) by the measurement of the energy loss (dE/dx) in the detector gas with a resolution of 6%. The other two TPCs (MTPCs) downstream of the magnets have large dimensions ($4 \times 4 \times 1.2$ m^3, 90 pad rows) and provide additional momentum resolution for high-momentum particles as well as PID by dE/dx measurement with a resolution of around 4%. A momentum resolution in the range $\sigma(p)/p^2 = (0.3–7) \times 10^{-4}$ (GeV/c)$^{-1}$ is achieved. Two time-of-flight scintillator arrays of 891 pixels each (TOF), situated just behind the MTPCs symmetrically on either side of the beam axis, add additional K/π separation power in the laboratory momentum range from 1 to 10 GeV/c (near mid-rapidity for kaons). A veto-calorimeter (VCAL) placed 20 m downstream of the target accepts all beam particles and projectile fragments as well as most of the spectator neutrons and protons [27]. The geometrical acceptance of the VCAL was readjusted for each beam energy by means of a collimator for optimum projectile spectator coverage. The VCAL is used for offline (online) selection of event centrality in Pb + Pb (C + C and Si + Si) collisions. The NA49 detector is described in detail in Ref. [27].

For Pb + Pb collisions a primary SPS beam of $40A$ GeV and $158A$ GeV was directed onto a Pb target while for C + C and Si + Si interactions a fragmented Pb beam of $40A$ GeV was used. The fragments were identified by magnetic rigidity ($Z/A = 0.5$) and by a pulse-height measurement in a scintillation counter in the beam. For C + C and Si + Si interactions beam particles with Z around 6 and Z around 14, respectively, were selected online. A refined Z selection was done offline, which yielded a pure C beam, whereas for the "Si beam" the different charges could not be separated well

enough, and thus a mixture of ions with $Z = 13$, 14, and 15 (with an intensity ratio of 34:44:22) were accepted. The target disks had thicknesses of 10 mm (carbon), 5 mm (silicon), and 200 μm (lead) corresponding to 7.9%, 4.4%, and 0.5% interaction lengths for the respective beam particles.

The Pb (light-ion) beam passed through a quartz Cherenkov (scintillator) detector, from which the start signal for the time-of-flight measurement was obtained, and three stations of multiwire proportional chambers, which measured the trajectory and energy loss of individual beam particles. A minimum-bias trigger for Pb + Pb interactions was derived from the signal of a gas Cherenkov device right behind the target. Only interactions which reduce the beam charge and thus the signal seen by this detector by at least 10% were accepted. The interaction cross section thus defined is 5.7 b at both energies. The trigger for the C + C and Si + Si data taking at 40A GeV was based on the energy deposited in the VCAL. The 66% most central C + C and 29% most central Si + Si interactions were selected by requiring an energy in the VCAL below the imposed threshold. These fractions are determined using the inelastic $A + A$ cross sections (10% uncertainty), the trigger cross sections (5% uncertainty), and a simulation of the VCAL response.

III. DATA ANALYSIS

The data sample used for this analysis was collected in specific minimum-bias runs of the NA49 experiment and thus are different from the central data presented earlier [2]. The recorded minimum-bias Pb + Pb collisions were divided into five consecutive centrality bins: C0–C4 (see Table I and Ref. [28]). The centrality selection is based on the forward-going energy of projectile spectators as measured in the VCAL. We quantify centrality by the fraction of cross section according to intervals of forward-going spectator energy. For each centrality interval a characteristic quantity, the mean

TABLE I. Overview of the analyzed data and centrality classes for minimum-bias Pb + Pb collisions. The centrality is given as fraction of the total inelastic cross section. $\langle N_{\mathrm{w}} \rangle$ is the average number of wounded nucleons per event, and N_{event} is the number of analyzed events.

E_{beam} (GeV)	Class	Centrality (%)	$\langle N_{\mathrm{w}} \rangle$	$N_{\mathrm{event}}/10^3$
40A	C + C	0–66	8.8 ± 1.1	135
40A	Si + Si	0–29	30.5 ± 3.5	65
40A	C0	0–5	356 ± 1	13
40A	C1	5–12.5	292 ± 2	23
40A	C2	12.5–23.5	212 ± 3	34
40A	C3	23.5–33.5	144 ± 4	33
40A	C4	33.5–43.5	93 ± 7	32
158A	C0	0–5	357 ± 1	15
158A	C1	5–12.5	288 ± 2	24
158A	C2	12.5–23.5	211 ± 3	37
158A	C3	23.5–33.5	146 ± 4	35
158A	C4	33.5–43.5	85 ± 7	35

value of "wounded nucleons," $\langle N_{\mathrm{w}} \rangle$, is calculated. A nucleon is considered wounded if its interaction occurs in the nuclear overlap volume. $\langle N_{\mathrm{w}} \rangle$ is determined by generating VCAL spectra with events from the VENUS 4.12 Monte Carlo code [29]. The simulation took into account the energy resolution of the calorimeter and contributions of participants to the energy recorded by the VCAL. After cross-calibration of experimental and simulated spectra for effects of the experimental trigger in the most peripheral centrality bin the mean number of interacting (wounded) nucleons ($\langle N_{\mathrm{w}} \rangle$) was extracted from the model data for each of the selected cross-section fractions [30]. The latter were selected to be identical at 40A GeV and 158A GeV. Thus only insignificant differences of $\langle N_{\mathrm{w}} \rangle$ are observed between the two energies except for the 10% discrepancy in the most peripheral centrality interval, which we attribute to the slightly different online trigger conditions. Table I summarizes these numbers together with the number of analyzed events. For convenience we quote here the centrality of the C + C and Si + Si collisions at 158 A GeV [8] which are used for comparison in this paper: the most central 15.3% ($\langle N_{\mathrm{w}} \rangle = 14 \pm 2$) and 12.2% ($\langle N_{\mathrm{w}} \rangle = 37 \pm 3$), respectively.

The recorded Pb + Pb events are contaminated by background due to nontarget interactions. This contamination was minimized by cuts on the fitted vertex position and the quality of the fit. It is negligible for near-central collisions and amounts to less than 5% for the most peripheral collisions (see [28]). Similar cuts were applied to the C + C and Si + Si collision events. Details for the latter are given in Table 4.1 of [31].

The track-finding efficiency and dE/dx resolution were optimized by track quality criteria, some of which are different for pions and kaons. These criteria are meant to select phase-space regions with low track densities, where the background and efficiency corrections are small and approximately uniform. Only those particles were considered for which the transverse momentum kick due to the magnetic field points in the same direction as the azimuthal angle projected onto the deflection plane. In addition the number of reconstructed points on the particle track had to exceed 50% of all measurable points. Further track cuts on azimuthal angles with respect to the bending plane and for a minimum of measured and/or measurable points are meant to obtain high-quality track samples. These track cuts were chosen differently for different particle species and data samples to optimize phase-space coverage: For negatively charged hadrons and kaons azimuthal angles within $\pm 30°$ with respect to the bending plane were selected, except for kaons in the C + C and Si + Si events, where angles of $\pm 45°$ were allowed to enhance statistics. Tracks of negatively charged hadrons in C + C and Si + Si events were required to have at least 10 potential points in the TPCs, while in Pb + Pb events a minimum of 30 measured points was asked for. Kaon tracks in C + C and Si + Si events had to have a minimum of 50 measured points in all TPCs and at least 1 potential point in the VTPCs. In Pb + Pb events they were required to have a minimum of 50 measured points in the MTPCs and at least 1 measured point in the VTPCs, if the number of measurable points was larger than 10. Finally, kaon candidate tracks in the sample of Pb + Pb events were required to point to the main

interaction vertex with a precision of 2 cm in the x (bending) direction and 1 cm in the y direction.

While kaon spectra were determined by means of particle identification, pion spectra were obtained by subtracting from all negatively charged particles the contributions from electrons, kaons, and antiprotons (see below). Kaons were identified using the energy loss (dE/dx) information from the TPCs and time-of-flight measurements in the phase space covered by the TOF walls. For the analysis based on dE/dx information alone, raw yields of K^+ and K^- were extracted from fits to the dE/dx distributions in bins of laboratory (p_{lab}) momentum (11 bins from 5 to 50 GeV/c in logarithmic scale for the 158A GeV data set and 10 bins from 4 to 32 GeV/c in logarithmic scale for the 40A GeV data set) and of transverse momentum (p_T) in 20 bins from 0 to 2 GeV/c in linear scale. See [32] for a detailed description of the fitting method. The energy loss information from the MTPCs (VTPCs and MTPCs) was used in the analysis of minimum-bias Pb + Pb (C + C and Si + Si) collisions. Bins with fewer than 500 particles were not used in the further analysis to ensure sufficient statistics for the fits to the dE/dx distributions. This cut limits the accessible range in p_T to values below 1 to 1.5 GeV/c depending on p_{lab}. The phase space in p_{lab} and thus the acceptance in rapidity y is limited by the fact that only for momenta from $p_{lab} = 4$ GeV/c to $p_{lab} = 50$ GeV/c is the mean energy loss of kaons sufficiently separated from those of pions and protons to allow for the extraction of their yield by unfolding of the dE/dx distributions. This restriction limits the acceptance of kaons to forward rapidities. The resulting distributions were corrected for geometrical acceptance, in-flight decay of kaons, and reconstruction efficiency. The first two corrections were determined by detector simulations using GEANT [33].

The reconstruction efficiency is track-density dependent only for Pb + Pb collisions. It was shown earlier [8] that the corrections are negligible for C + C and Si + Si interactions. The correction factor was determined by embedding simulated tracks into real events in three centrality bins ranging from 0% to 12.5%, 12.5% to 33.5%, and >33.5%. Track losses are of order 5%–10% for central collisions at 158A GeV and drop to only 1%–2% in the most peripheral collisions and for 40A GeV beam energy. Systematic errors were determined by varying track selection criteria and the parameters in the dE/dx unfolding procedure. In particular, we decreased the minimum number of measured points from 50 to 30 and used an azimuthal cut of $\pm50°$ instead of $\pm30°$. The asymmetry parameter in the dE/dx unfolding procedure, which accounts for the asymmetry of the distributions of the truncated mean (for details see [32]), was varied within the limits 0.6 and 0.8. Different combinations of these parameter settings resulted in the systematic errors indicated in Tables II and III. The spectra at mid-rapidity were obtained by using the combined dE/dx and TOF information (Pb + Pb only; statistics were not sufficient for C + C and Si + Si). The distributions of m^2 calculated from the recorded time of flight ($\sigma_{TOF} \sim 65$ ps) were parametrized in bins of laboratory momentum as the sum of three Gaussians for pions, kaons, and protons plus exponential tails stemming from unresolved double hits or coincidence with γ conversion in the scintillators. For laboratory momenta below 2.5 GeV/c, this measurement is sufficient to separate kaons from pions and protons with high efficiency (~ 95%) and high purity (>96%). For higher momenta, the independent measurements of time of flight and specific energy loss are used simultaneously. In the two-dimensional plane of m^2 and dE/dx, kaons were identified by an elliptical region centered at the expectation values and with half-axes equal to $2.5\sigma_{m^2}$

TABLE II. Summary of data for pion and kaon production in centrality selected Pb + Pb collisions at 158A GeV beam energy: rapidity density dN/dy at mid-rapidity [π^-: $0 < y < 0.4$, $K^\pm$: average of result from TOF analysis ($-0.2 < y < 0.2$) and dE/dx analysis ($0.1 < y < 0.3$)], total multiplicity $\langle N \rangle$, rms width of the rapidity distribution, RMS_y, average transverse mass at mid-rapidity, $\langle m_T \rangle - m_0$, inverse slope parameter of m_T spectra at mid-rapidity [π^-: $0 < y < 0.2$, fit range $0.2 < m_T - m_0 < 0.7$ GeV/c^2; $K^\pm$: $-0.2 < y < 0.2$ (TOF analysis), fit range $0 < m_T - m_0 < 1.0$ GeV/c^2]. The first error is statistical, and the second is systematic.

	Centrality class	dN/dy	$\langle N \rangle$	RMS_y	$\langle m_T \rangle - m_0$ (MeV/c^2)	T (MeV)
π^-	0	$158.8 \pm 0.7 \pm 16$	$602 \pm 4.7 \pm 42$	$1.39 \pm 0.01 \pm 0.07$	$281 \pm 2 \pm 28$	$184 \pm 2 \pm 9$
	1	$121.4 \pm 0.6 \pm 8.5$	$480 \pm 4.5 \pm 29$	$1.44 \pm 0.01 \pm 0.07$	$287 \pm 2 \pm 28$	$187 \pm 1 \pm 9$
	2	$86.2 \pm 0.5 \pm 4.3$	$349 \pm 4.2 \pm 17$	$1.49 \pm 0.01 \pm 0.08$	$282 \pm 2 \pm 28$	$180 \pm 1 \pm 9$
	3	$57.2 \pm 0.4 \pm 2.9$	$237 \pm 3.8 \pm 12$	$1.55 \pm 0.02 \pm 0.08$	$280 \pm 2 \pm 28$	$178 \pm 2 \pm 9$
	4	$37.2 \pm 0.3 \pm 1.9$	$159 \pm 3.4 \pm 7.9$	$1.61 \pm 0.02 \pm 0.08$	$275 \pm 2 \pm 28$	$177 \pm 2 \pm 9$
K^+	0	$28.35 \pm 0.43 \pm 2.9$	$97.8 \pm 3 \pm 9.8$	$1.15 \pm 0.02 \pm 0.06$	$305 \pm 6 \pm 15$	$232 \pm 3 \pm 12$
	1	$22.72 \pm 0.31 \pm 2.3$	$78.5 \pm 2.8 \pm 7.8$	$1.17 \pm 0.02 \pm 0.06$	$302 \pm 5 \pm 15$	$229 \pm 3 \pm 12$
	2	$15.86 \pm 0.23 \pm 1.6$	$57.1 \pm 2.9 \pm 5.7$	$1.18 \pm 0.02 \pm 0.06$	$300 \pm 5 \pm 15$	$227 \pm 2 \pm 12$
	3	$10.01 \pm 0.17 \pm 1.0$	$34.9 \pm 2 \pm 3.5$	$1.21 \pm 0.02 \pm 0.06$	$283 \pm 6 \pm 14$	$215 \pm 3 \pm 11$
	4	$6.39 \pm 0.13 \pm 0.6$	$23.2 \pm 1.9 \pm 2.3$	$1.22 \pm 0.02 \pm 0.06$	$277 \pm 7 \pm 14$	$209 \pm 3 \pm 11$
K^-	0	$16.8 \pm 0.43 \pm 1.7$	$53.95 \pm 2.15 \pm 4.3$	$1.12 \pm 0.03 \pm 0.06$	$298 \pm 9 \pm 15$	$225 \pm 5 \pm 11$
	1	$13.38 \pm 0.24 \pm 1.3$	$43.18 \pm 2.03 \pm 3.5$	$1.15 \pm 0.03 \pm 0.06$	$294 \pm 7 \pm 15$	$221 \pm 4 \pm 11$
	2	$9.54 \pm 0.17 \pm 0.9$	$31.32 \pm 2.03 \pm 2.5$	$1.25 \pm 0.1 \pm 0.06$	$285 \pm 8 \pm 14$	$217 \pm 3 \pm 11$
	3	$6.26 \pm 0.12 \pm 0.6$	$20.45 \pm 1.69 \pm 1.6$	$1.29 \pm 0.03 \pm 0.07$	$273 \pm 8 \pm 14$	$210 \pm 4 \pm 11$
	4	$3.92 \pm 0.11 \pm 0.4$	$12.24 \pm 1.18 \pm 1.2$	$1.21 \pm 0.07 \pm 0.06$	$264 \pm 10 \pm 13$	$202 \pm 5 \pm 10$

TABLE III. Summary of data for pion and kaon production in centrality selected Pb + Pb collisions at $40A$ GeV beam energy: rapidity density dN/dy at mid-rapidity [π^-: $0 < y < 0.4$, K$^\pm$: result from TOF analysis ($-0.1 < y < 0.1$)], total multiplicity $\langle N \rangle$, rms width of the rapidity distribution, RMS_y, average transverse mass at mid-rapidity, $\langle m_T \rangle - m_0$, inverse slope parameter of m_T spectra at mid-rapidity [π^-: $0 < y < 0.2$, fit range 0.2 GeV/$c^2 < m_T - m_0 < 0.7$ GeV/c^2; K$^\pm$: $-0.1 < y < 0.1$ (TOF analysis), fit range $0 < m_T - m_0 < 0.8$ GeV/c^2]. The first error is statistical, and the second is systematic.

	Centrality class	dN/dy	$\langle N \rangle$	RMS_y	$\langle m_T \rangle - m_0$ (MeV/c^2)	T (MeV)
π^-	0	$118 \pm 0.6 \pm 12$	$348 \pm 2.4 \pm 17.4$	$1.11 \pm 0.01 \pm 0.06$	$270 \pm 3 \pm 27$	$172 \pm 3 \pm 9$
	1	$93.8 \pm 0.5 \pm 9.4$	$286 \pm 2.4 \pm 14.3$	$1.15 \pm 0.01 \pm 0.06$	$272 \pm 3 \pm 27$	$172 \pm 3 \pm 9$
	2	$67.8 \pm 0.4 \pm 6.8$	$214 \pm 2.4 \pm 10.7$	$1.19 \pm 0.01 \pm 0.06$	$273 \pm 2 \pm 27$	$178 \pm 2 \pm 9$
	3	$43.7 \pm 0.3 \pm 4.4$	$146.3 \pm 2.2 \pm 7.3$	$1.25 \pm 0.01 \pm 0.06$	$269 \pm 3 \pm 27$	$172 \pm 3 \pm 9$
	4	$29.1 \pm 0.2 \pm 2.9$	$101.1 \pm 1.9 \pm 10$	$1.29 \pm 0.01 \pm 0.06$	$263 \pm 3 \pm 26$	$168 \pm 3 \pm 9$
K^+	0	$20.1 \pm 0.6 \pm 1.9$	$60.0 \pm 4.7 \pm 4.8$	$1.00 \pm 0.02 \pm 0.05$	$312 \pm 13 \pm 15$	$238 \pm 7 \pm 12$
	1	$16.2 \pm 0.4 \pm 1.5$	$49.1 \pm 4.3 \pm 3.9$	$1.05 \pm 0.02 \pm 0.05$	$307 \pm 11 \pm 15$	$238 \pm 6 \pm 12$
	2	$10.9 \pm 0.3 \pm 1.0$	$34.2 \pm 3.5 \pm 2.7$	$1.03 \pm 0.01 \pm 0.05$	$309 \pm 12 \pm 15$	$234 \pm 6 \pm 12$
	3	$6.9 \pm 0.2 \pm 0.7$	$22.0 \pm 2.8 \pm 1.7$	$1.06 \pm 0.02 \pm 0.05$	$291 \pm 14 \pm 15$	$221 \pm 7 \pm 11$
	4	$4.2 \pm 0.2 \pm 0.4$	$13.6 \pm 2.3 \pm 1.4$	$1.08 \pm 0.03 \pm 0.05$	$265 \pm 16 \pm 13$	$208 \pm 9 \pm 11$
K^-	0	$8.5 \pm 0.3 \pm 0.7$	$21.0 \pm 3.1 \pm 2$	$0.89 \pm 0.03 \pm 0.05$	$323 \pm 19 \pm 15$	$239 \pm 10 \pm 12$
	1	$6.2 \pm 0.2 \pm 0.5$	$15.9 \pm 2.7 \pm 1.3$	$0.91 \pm 0.03 \pm 0.05$	$294 \pm 16 \pm 15$	$231 \pm 9 \pm 12$
	2	$4.7 \pm 0.2 \pm 0.4$	$11.4 \pm 2.3 \pm 0.9$	$0.89 \pm 0.04 \pm 0.05$	$304 \pm 16 \pm 15$	$227 \pm 8 \pm 12$
	3	$2.7 \pm 0.1 \pm 0.2$	$7.0 \pm 1.8 \pm 0.6$	$0.88 \pm 0.03 \pm 0.05$	$275 \pm 20 \pm 14$	$207 \pm 10 \pm 11$
	4	$2.0 \pm 0.1 \pm 0.2$	$4.6 \pm 1.5 \pm 0.5$	$0.85 \pm 0.04 \pm 0.05$	$291 \pm 24 \pm 15$	$219 \pm 14 \pm 11$

and $2.5\sigma_{dE/dx}$, respectively. In addition, regions where the local kaon contribution, according to the parametrizations of m^2 and dE/dx, is below 0.7 were excluded. Each track in the kaon identification area entered the transverse momentum spectrum with a specific weight accounting for the efficiency of particle identification and for the efficiency of the time-of-flight detector. The identification efficiency is defined by the ratio of the integral of the two-dimensional kaon distribution in m^2 and dE/dx inside the identification area to its total integral. It does not depend on the centrality class and is determined as a function of track momentum. For the kaon identification employed here, the efficiency is about 95% and varies only slightly with momentum. The contamination by pions and protons is below 1% for all momenta and is not corrected for. Efficiency losses of the time-of-flight detectors are caused by multiple hits in one scintillator and quality cuts on the deposited charge. They were determined from the data themselves for each channel and in each centrality class separately. The average efficiency is 82% and varies slightly with centrality. Finally, the transverse mass spectra were corrected for the geometrical acceptance and the in-flight kaon decay, which was obtained by a detector simulation with GEANT.

The separation of negatively charged pions from kaons and antiprotons in the acceptance of the NA49 detectors by means of the energy loss measurement is limited to high transverse momenta (p_T larger than 500 MeV/c at mid-rapidity and larger than 200 MeV/c at $y_{cm} = 1$ for $158A$ GeV beam energy). Therefore a different method was chosen for the evaluation of π^- production (see [3]). Yields of all negatively charged hadrons (h$^-$) from the primary vertex were extracted in bins of rapidity and p_T by assuming the pion mass. The contamination by K$^-$, $\bar{p}$, and e^- and by particles from the decay of strange

particles and from secondary interactions, both reconstructed at the primary vertex, was estimated by simulation and subtracted. The calculation of theses corrections is based on events generated by the VENUS model [29], propagated through the NA49 detector using GEANT, and processed by the standard reconstruction chain. The ratio of reconstructed to all simulated particles yields correction factors in all bins of rapidity and p_T which account for all background tracks in the negatively charged hadron yields. Care was taken to account for differences between simulated and measured hadron yields by appropriate scaling factors. These were obtained from a comparison of the simulated yields with measured data. Where measured yields are not available, particle ratios from statistical model calculations were used to infer the corresponding yields. In general, distributions of background particles from VENUS events were scaled by a global factor. The largest corrections to the pion yields arise from K$^-$ in Pb + Pb collisions ($158A$ GeV) at high p_T (30% for $p_T > 1.2$ GeV/c) where pion yields are low and kaons prevail. The K$^-$ distributions were therefore scaled differentially (and iteratively) in rapidity and p_T in order to reproduce the shapes of the measured spectra. The differences in the correction factors on the negatively charged particles from K$^-$ was found to be in the range of 1%–3%. As this is a very small change, we found it justified to use global factors for the other contributions. At mid-rapidity and low p_T (<0.1 GeV/c) corrections amount to 30%–40% due to contributions from (secondary) electrons ($158A$ GeV). This large correction requires a careful evaluation as the contribution relies fully on the GEANT calculation. We therefore identified and removed electrons from the track samples in both the simulation and in the data (for the latter based on dE/dx measurements). Results agree within 5%–10% in the corresponding bins of

rapidity and transverse momentum and within 2%–3% for the overall pion yield. For the overall evaluation of systematic errors on the pion yield we performed further analyses with different track selection parameters (with a minimum of 50 instead of 30 measured points), reversed magnetic field, and a different data set with slightly varied settings for the online selection of minimum-bias events. Variations of the pion yield are less than 5% in centrality bins C0–C3 and 10% in bin C4. This higher error in the latter bin is due to the uncertainty of the event selection for the most peripheral bin. In C + C and Si + Si collisions at $40A$ GeV π^- were analyzed with both methods (h^- and dE/dx). The differences were found to be below 5%.

The subtraction method is not well suited for the determination of the π^+ yields at our energies, because positively charged particles have a large contribution of protons. However, for Pb + Pb collisions yields at mid-rapidity and full phase space can be inferred using the feed-down-corrected π^+/π^- ratio from the combined dE/dx and TOF analysis in an acceptance which is a banana-shaped region in the rapidity-p_T plane within $0 < p_T < 1400$ MeV/c and $2.1 < y < 3.1$ ($0 < p_T < 1300$ MeV/c and $2.5 < y < 5.0$) at $40A$ GeV ($158A$ GeV). This method relies on the assumption that the p_T and rapidity distributions of π^- and π^+ have the same shapes. In VENUS events this assumption leads to differences of 2% between the direct and scaled π^+ multiplicities. The extracted π^+/π^- ratios are 0.93 ± 0.2 and 0.90 ± 0.1 at $158A$ GeV and $40A$ GeV beam energies, respectively, and are subject to a 4% systematic uncertainty, which is derived from the difference between two different methods (see [2,3]). We assume that this ratio is centrality independent. For C + C and Si + Si collisions the π^-/π^+ ratios were determined at $158A$ GeV beam energy (0.99 and 1.02) in [8]. We use these same values at $40A$ GeV. More details on the analysis of minimum-bias Pb + Pb collisions can be found in [34]. The C + C and Si + Si analyses of pion and kaon yields at $40A$ GeV are described in [31,35], respectively.

IV. RESULTS

A. Transverse mass spectra

Transverse mass spectra at mid-rapidity are shown in Figs. 1 and 2 for kaons (combined dE/dx and TOF analysis) and pions for different centrality classes in Pb + Pb collisions at $40A$ GeV and $158A$ GeV beam energy. Figure 3 presents results for kaons and pions near mid-rapidity in C + C and Si + Si collisions at $40A$ GeV. The m_T spectra ($m_T = \sqrt{(m^2 + p_T^2)}$) were fitted by an exponential function with inverse slope T:

$$\frac{dN}{m_T dm_T dy} = C \exp\left(-\frac{m_T}{T}\right) \quad (1)$$

in $m_T - m_0$ ranges as given in the figure captions. In Pb + Pb collisions the transverse mass spectra of kaons are well described by this functional form, while pion spectra deviate at high and low transverse masses. The m_T spectra of kaons in the light systems exhibit a two to three times statistical error downward deviation at low m_T. For a model-independent study of the transverse mass spectra, the average transverse
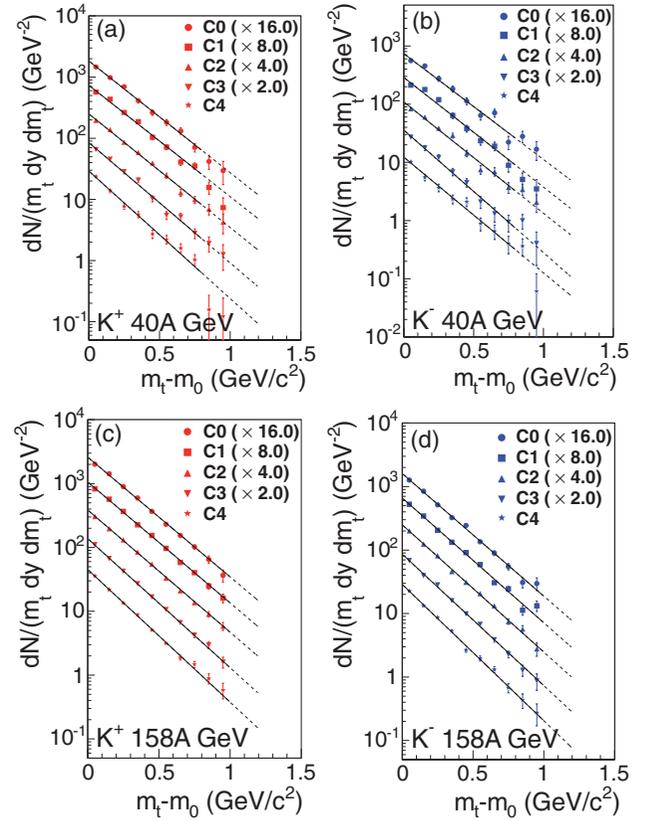

FIG. 1. (Color online) Transverse mass spectra at mid-rapidity from the combined dE/dx and TOF analysis for K$^+$ and K$^-$ in Pb + Pb collisions at $40A$ GeV ($-0.1 < y < 0.1$) and $158A$ GeV ($-0.2 < y < 0.2$) beam energy. Lines show exponential fits for 0.0 GeV/$c^2 < m_T - m_0 < 0.8$ GeV/c^2 ($40A$ GeV) and 0.0 GeV/$c^2 < m_T - m_0 < 1.0$ GeV/c^2 ($158A$ GeV). Different centralities are scaled for clarity. The error bars indicate the statistical uncertainty.

mass $\langle m_T \rangle - m_0$ was therefore calculated. To account for the small unmeasured high m_T part of the kaon spectra, which is on a percent level only, the spectra were extrapolated by the exponential functions shown in Figs. 1 and 3. For the pion spectra in Pb + Pb collisions an exponential function with two slope parameters was used (not shown), to account for the concave shape of the distributions (in logarithmic representation). An estimate of systematic errors was derived from using different fit ranges for the extrapolation or a single exponential for pions. The resulting average transverse masses and inverse slope parameters are summarized in Tables II, III, and IV. Figure 4 shows the dependence of $\langle m_T \rangle - m_0$ on the mean number of wounded nucleons, $\langle N_w \rangle$, for the investigated collision systems at $40A$ GeV and $158A$ GeV beam energy. Results from central Pb + Pb collisions [2,3], $p + p$ collisions at 158 GeV/c [10], and C + C and Si + Si collisions [8] at $158A$ GeV are also shown.

Owing to the mass difference and well-known radial flow effect, $\langle m_T \rangle - m_0$ values are larger for kaons than for pions. For central collisions [2,3] mean transverse masses do not change significantly from $40A$ GeV to $158A$ GeV. For pions, if any, only a weak centrality dependence is observed at $40A$ GeV and none at $158A$ GeV beam energy, while kaons
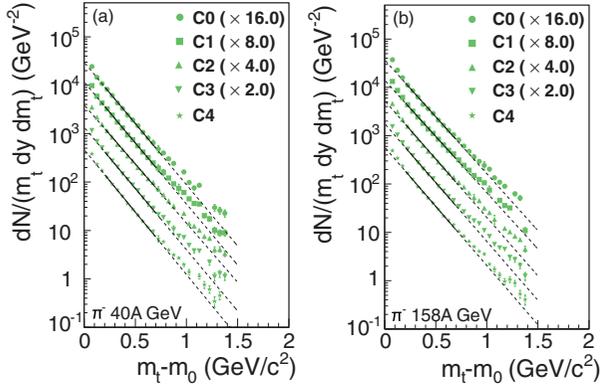
FIG. 2. (Color online) Transverse mass spectra at mid-rapidity $(0 < y < 0.2)$ for π^- in Pb + Pb collisions at $40A$ GeV and $158A$ GeV beam energy. Lines show exponential fits for $0.2 < m_T - m_0 < 0.7$ GeV/c^2. Different centralities are scaled for clarity. The error bars indicate the statistical uncertainty.

show an increase of mean transverse masses toward central Pb + Pb collisions. This increase is particularly pronounced when comparing to the much smaller C + C and Si + Si collision systems with $\langle N_w \rangle < 60$.

B. Rapidity spectra

Transverse momentum spectra were measured in bins of rapidity in order to extract the rapidity dependence of p_T-integrated yields. The measured p_T spectra were extrapolated into unmeasured regions by a single exponential for both kaons and pions in C + C and Si + Si interactions. A double exponential had to be used for pions in Pb + Pb collisions because of the concave shape of their p_T spectra. Rapidity distributions of p_T-integrated yields for the particles, collision systems, and energies under study are shown in Figs. 5, 6, 7, and 8. They are well described by two Gaussians of equal widths σ which are displaced symmetrically around mid-

rapidity by a constant y_0:

$$\frac{dN}{dy} = C \left[\exp\left(-\frac{(y - y_0)^2}{2\sigma_y^2} \right) + \exp\left(-\frac{(y + y_0)^2}{2\sigma^2} \right) \right]. \quad (2)$$

By using this functional form the measured rapidity spectra can be extrapolated into the unmeasured regions, and particle yields in full phase space can be extracted. For C + C and Si + Si collisions at $40A$ GeV beam energy no combined dE/dx and TOF measurement is available at mid-rapidity. The resulting uncertainties in the shapes and integrals of the rapidity distributions of kaons were evaluated by applying three different fit functions [Eq. (2)]: with two free parameters (σ_y and y_0), with these parameters fixed to values obtained from fits to the corresponding distributions from central Pb + Pb collisions at $40A$ GeV, and with a single Gaussian with its root mean square (rms) again taken from the $40A$ GeV Pb + Pb data. These fits are indicated in Fig. 8 by the solid, short-dashed, and dashed lines and were used to extrapolate into the unmeasured rapidity regions. Differences in the total yields between extremes do not exceed 12% and are included in the systematic errors. The quoted total and mid-rapidity yields are the means of the values obtained from the three fits. The widths of the rapidity distributions are quantified by $RMS_y = \sqrt{\sigma_y^2 + y_0^2}$. These values are tabulated together with mid-rapidity and full phase-space yields in Tables II, III, and IV. Figure 9 presents the system-size dependence of the widths of the rapidity distributions. While kaons show no significant change of the width as a function of the number of wounded nucleons, rapidity distributions of pions are significantly wider in peripheral than in central Pb + Pb collisions. In fact, it turns out that the width of the pion rapidity distribution in central Pb + Pb collisions is the same as in C + C and Si + Si reactions as well as in $p + p$ interactions at 158 GeV/c. Only noncentral Pb + Pb collisions deviate from this common behavior exhibiting a wider distribution. The widening of the pion rapidity distribution for peripheral collisions is probably due to pion production in interactions of participants with spectator matter, which had been already
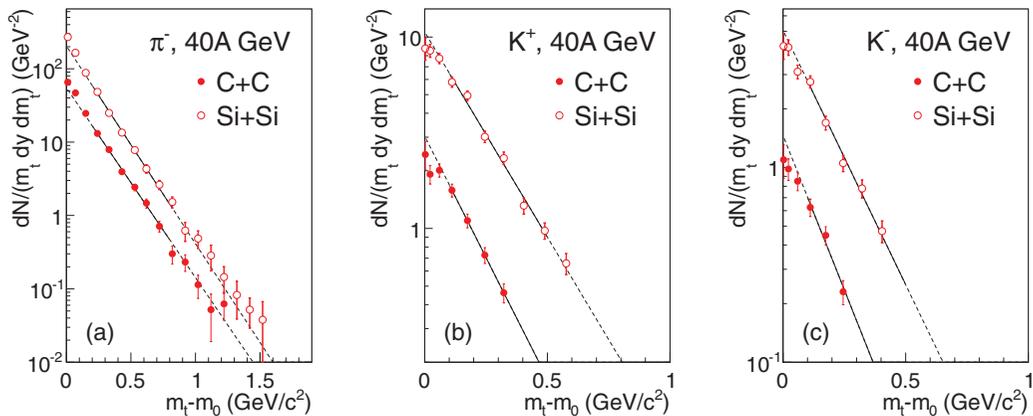

FIG. 3. (Color online) Transverse mass spectra of π^- $(0 < y < 0.2)$ and kaons $(0.8 < y < 1.0)$ at $40A$ GeV in C + C and Si + Si collisions. Lines show exponential fits for 0.2 GeV/$c^2 < m_T - m_0 < 0.8$ GeV/c^2 (π^-) and 0.1 GeV/$c^2 < m_T - m_0 < 0.5$ GeV/c^2 (kaons). The inverse slope parameters for K$^+$(K$^-$) are 171 ± 18 MeV for C + C and 203 ± 10 MeV for Si + Si collisions (137 ± 24 MeV for C + C and 166 ± 13 MeV for Si + Si collisions). The inverse slopes of pions are given in Table IV. The error bars indicate the statistical uncertainty.

TABLE IV. Summary of data for pion and kaon production in C + C and Si + Si collisions at $40A$ GeVbeam energy: rapidity density dN/dy at mid-rapidity (π^-: $0 < y < 0.4$, $K^\pm$: $y = 0$ average of the three fit functions), their multiplicities $\langle N \rangle$, and the rms widths, RMS_y, of their rapidity distributions. For pions also average transverse masses $\langle m_T \rangle - m_0$ and the inverse slope parameters T of the m_T spectra are given ($0 < y < 0.2$, fit range $0.2 < m_T - m_0 < 0.7$ GeV/c^2). The first error is statistical, and the second is systematic. The systematic errors on the yields are 15%.

	Collision	dN/dy	$\langle N \rangle$	RMS_y	$\langle m_T \rangle - m_0$ (MeV/c^2)	T (MeV)
π^-	C + C	3.25 ± 0.06	10.0 ± 1.4	$1.18 \pm 0.04 \pm 0.1$	$247 \pm 11 \pm 25$	$169 \pm 8 \pm 9$
	Si + Si	11.40 ± 0.19	34.6 ± 2.7	$1.16 \pm 0.03 \pm 0.1$	$243 \pm 10 \pm 24$	$162 \pm 6 \pm 9$
K^+	C + C	0.46 ± 0.06	1.26 ± 0.78	$1.10 \pm 0.11 \pm 0.15$		
	Si + Si	1.82 ± 0.30	5.1 ± 1.2	$1.01 \pm 0.15 \pm 0.15$		
K^-	C + C	0.19 ± 0.02	0.44 ± 0.4	$0.80 \pm 0.08 \pm 0.12$		
	Si + Si	0.87 ± 0.07	2.0 ± 1.0	$0.89 \pm 0.09 \pm 0.12$		

invoked to explain the proton rapidity spectra in the same data sets [7].

C. Particle yields

Figure 10 shows the system-size dependence of particle yields normalized to the mean number of wounded nucleons. Earlier data on central C + C, Si + Si, and Pb + Pb collisions are plotted as well [2,3,8]. Data for $p + p$ collisions are taken from NA49 where available [9,10] and from parametrizations by Rossi *et al.* [38]. (The latter were used in the core-corona calculations; see below.) At 40 GeV/c we include results from a new study of the energy dependence of kaon

FIG. 4. (Color online) Mean transverse mass as extracted from the transverse mass spectra at mid-rapidity for π^-, K^+, and K^- vs number of participating nucleons. Open symbols show results from $p + p$, C + C, Si + Si, and central Pb + Pb collisions. Except for the new results for C + C and Si + Si collisions at $40A$ GeV beam energy the data are taken from [2,3,8–10]. Filled symbols represent the centrality selected Pb + Pb data. The thin vertical bars indicate the statistical errors, which are mostly not visible. The thick shaded bars indicate the systematic errors.

production in $p + p$ interactions reported in [10]. Also shown are calculations by the HSD [36] and UrQMD2.3 [37] transport models, as well as by the core-corona model (the latter for the Pb + Pb collision system only; see also Fig. 12) [39]. Normalized pion yields are rather independent of centrality or system size while the normalized yields of kaons show a steep increase for small system sizes followed by a slow rise or even saturation for higher centralities. The normalization to the mean number of wounded nucleons ($\langle N_w \rangle$) introduces a model dependence in these ratios, in particular for small systems, as for the semicentral C + C and Si + Si collisions the calculations have large uncertainties. Yields are therefore alternatively normalized to the number of pions. In Fig. 11 these ratios are presented. Normalized kaon yields at both energies exhibit the same dependence as seen in Fig. 10. A closer look reveals that at $158A$ GeV the K/π ratios in the small collision systems C + C and Si + Si seem to follow the trend set by the centrality dependence of the Pb + Pb data, whereas at $40A$ GeV the normalized kaon abundance in peripheral Pb + Pb collisions is lower than expected from the extrapolation of the K/π ratio in C + C and Si + Si collisions.
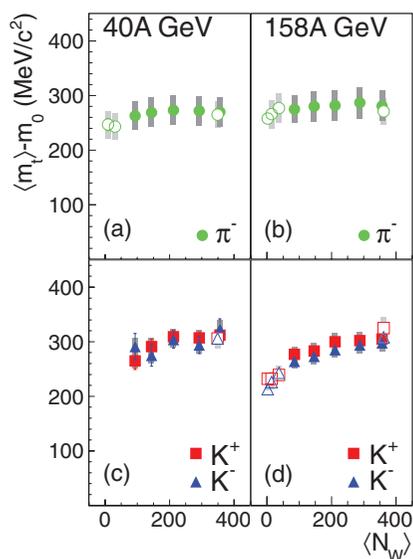
V. DISCUSSION

A. Comparison to transport models (HSD and UrQMD)

The centrality of the events generated by the models was derived from the corresponding fraction of the total (geometrical) cross section with the impact parameter as order parameter. The corresponding $\langle N_w \rangle$ values were those derived from the experimental data for HSD. For the UrQMD2.3 events the number of nucleons in the nuclear overlap volume, $\langle N_w \rangle$, was calculated event by event based on the chosen impact parameter. Pion rapidity distributions (Fig. 5) are well reproduced by both models at $40A$ GeV, whereas their predictions give slightly higher yields than the data at $158A$ GeV. For K^+ mesons (Fig. 6) the distributions from both models are 20% low at $40A$ GeV. For kaons at $158A$ GeV HSD calculations agree well with experiment, whereas UrQMD2.3 underestimates our data. The overall agreement between model calculations and data for the K^- mesons (Fig. 7) is generally good for both
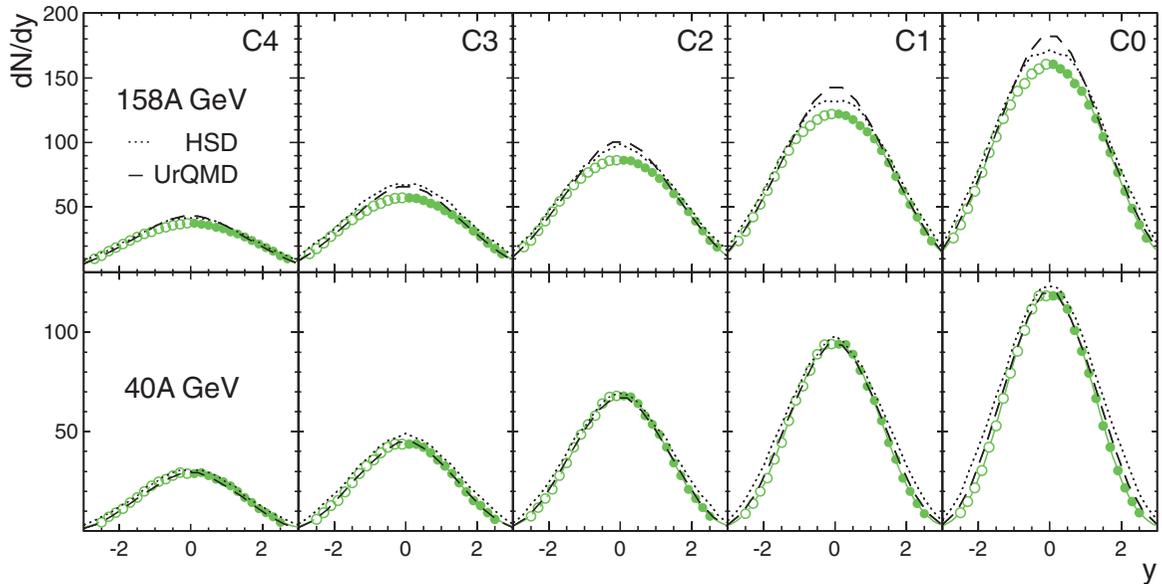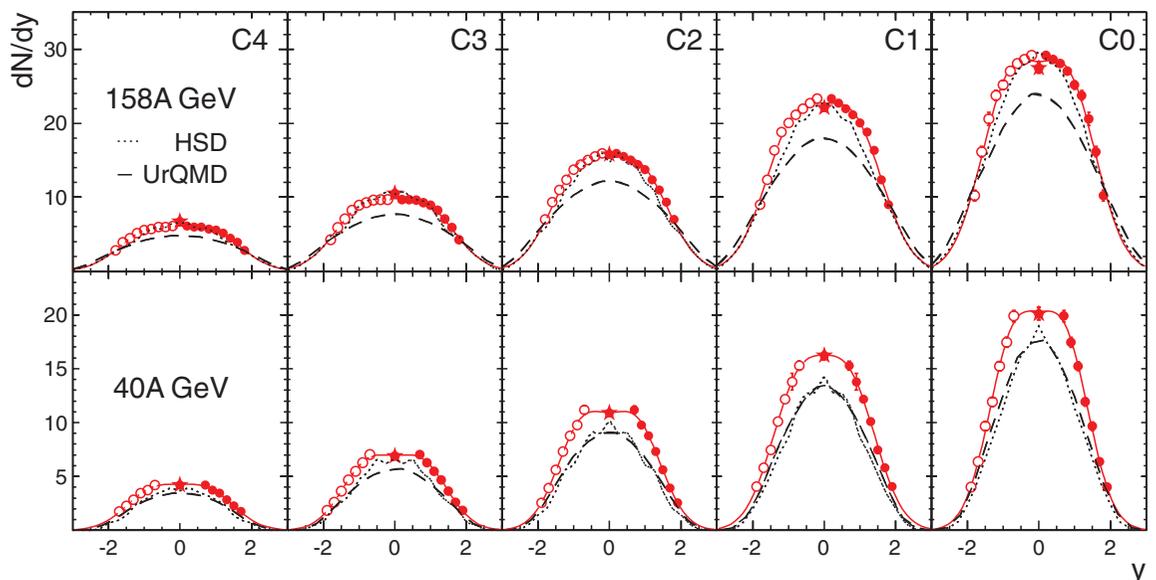
FIG. 5. (Color online) Rapidity spectra for π^- in Pb + Pb collisions at 40A GeV and 158A GeV beam energy for different centrality bins labeled C0–C4. Open symbols are reflected at mid-rapidity. Solid lines represent the fits of Eq. (2) (often not visible due to symbol size). The dotted and dashed lines represent HSD [36] and UrQMD2.3 [37] simulations, respectively. The error bars (mostly not visible) indicate the statistical uncertainty.

models, even though there is a small underestimation of the data by UrQMD2.3 at 158A GeV and by HSD at 40A GeV. No model data were provided for comparison to our C + C and Si + Si data. As to the shapes of the rapidity distributions both models describe well the increase of RMS_y with increasing impact parameter at both energies (Fig. 9). This increase is most (least) pronounced for the pions (K$^-$). We interpret this

rise as due to interactions of fireball particles with spectator remnants.

Normalized multiplicities are studied in Figs. 10 and 11. $\langle N \rangle / \langle N_w \rangle$ for pions is reproduced by UrQMD2.3 at both energies. HSD is 10% high, which is due to larger widths rather than higher amplitudes of the corresponding dN/dy distributions (cf. Fig. 5). We now turn to the normalized yields

FIG. 6. (Color online) Rapidity spectra of K$^+$ in Pb + Pb collisions at 40A GeV and 158A GeV beam energy for different centrality bins labeled C0–C4. Circles are values from the dE/dx analysis; the stars give the results from the combined dE/dx and TOF analyses. Open symbols are reflected at mid-rapidity. Solid lines represent the fits of Eq. (2) (often not visible due to symbol size). The dotted and dashed lines represent HSD [36] and UrQMD2.3 [37] simulations, respectively. The error bars (mostly not visible) indicate the statistical uncertainty.
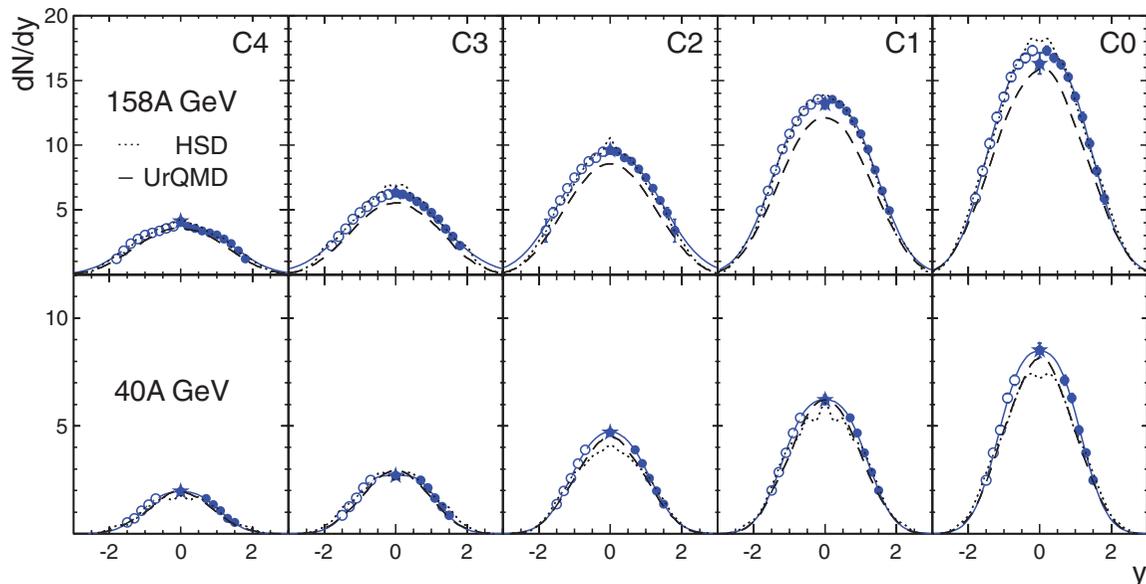
FIG. 7. (Color online) Rapidity spectra of K^- in Pb + Pb collisions at $40A$ GeV and $158A$ GeV beam energy for different centrality selections labeled C0–C4. Circles are values from the dE/dx analysis; the stars give the results from the combined dE/dx and TOF analysis. Open symbols are reflected at mid-rapidity. Solid lines represent the fits of Eq. (2). The dotted and dashed lines represent HSD [36] and UrQMD2.3 [37] simulations, respectively. The error bars (mostly not visible) indicate the statistical uncertainty.

of the K^+ meson. At $40A$ GeV the results from both models are low by 20%. At $158A$ GeV HSD results agree with our data, wheras UrQMD2.3 results underpredict them. The K^- yields are well described by both models at $40A$ GeV. At $158A$ GeV K^- meson yields are reproduced by HSD, whereas they are underpredicted by UrQMD2.3 as was the case for K^+ yields. The calculations of both models for the kaon to pion ratios yield values which are lower than the experimental data at both energies (see Fig. 11), although for different reasons. While UrQMD2.3 mainly underpredicts the kaon yields, HSD overpredicts the pions yields (see Figs. 10).

B. Transverse mass distributions and thermal freeze-out

Both the thermal freeze-out temperature and radial flow affect the observed m_T distributions of produced particles. The centrality dependence of $\langle m_T \rangle - m_0$ (near mid-rapidity), which is shown in Fig. 4, exhibits a clear trend of an increase of $\langle m_T \rangle - m_0$ with centrality (for Pb + Pb) and system size ($p + p$ and light versus heavy systems), which is most pronounced for kaons of both charges at $158A$ GeV. This finding is consistent with the picture that nuclear stopping and thus energy deposition increases with increasing centrality and from small to large collision systems, giving rise to higher temperatures or collective radial flow or both.

C. System-size dependence of the K/π ratio

The system-size dependence of the K/π ratios (see Fig. 11) hints at a behavior expected for the core-corona ansatz [39]. However, at $40A$ GeV there are significant deviations of the core-corona calculations from the experimental data. In

peripheral Pb + Pb collisions the data tend to be below the model values, being most pronounced for K^-, and the ratios measured for the small collision system (C + C and Si + Si) tend to be above the values calculated for the Pb + Pb system. The latter finding is in line with the model prediction for different system sizes as shown in Fig. 12. It shows the core fraction obtained in the core-corona model for different collision systems as a function of the number of participating nucleons [39]. Central collisions of small projectiles reach
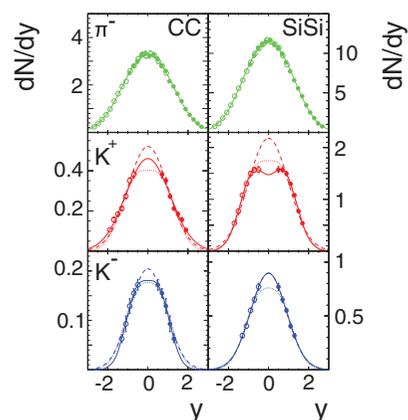

FIG. 8. (Color online) Rapidity spectra for π^- and $K^\pm$ for semicentral C + C and Si + Si collisions at $40A$ GeV beam energy. Solid lines show free fits of double Gaussians. Open symbols are reflected at mid-rapidity. For $K^\pm$ also double Gaussians with width σ and shift y_0 as for central Pb + Pb collisions at $40A$ GeV beam energy were fitted (short dashed line) as well as a single Gaussian with the same RMS_y (dashed line). The error bars indicate the statistical uncertainty.

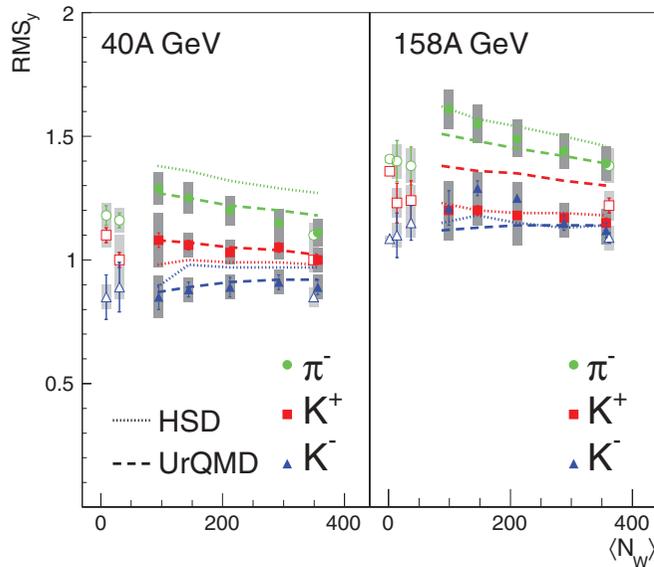FIG. 9. (Color online) Width of the rapidity distribution described by the rms values for π^-, K^+, and K^- vs mean number of participating nucleons. Open symbols show results from $p + p$, C + C, Si + Si, and central Pb + Pb collisions. Except for the new results for C + C and Si + Si collisions at $40A$ GeV beam energy the data are taken from [2,3,8,9]. Filled symbols represent the centrality selected Pb + Pb data. Lines show results from HSD [36] and UrQMD2.3 [37] simulations as indicated in the figure. The thin vertical bars indicate the statistical errors, which are mostly not visible. The thick shaded bars indicate the systematic errors.
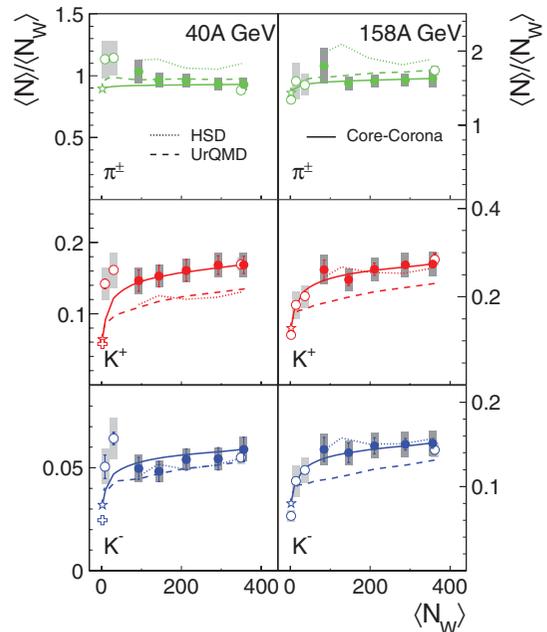

FIG. 10. (Color online) Particle yields divided by the mean number of wounded nucleons as a function of centrality. Closed symbols show results from centrality selected Pb + Pb collisions; open circles show $p + p$ data from NA49 [9,10] as well as C + C, Si + Si (at $158A$ GeV [8]), and central Pb + Pb collisions from [2,3]. The stars denote the values obtained for $p + p$ interactions from parametrization "B" in Ref. [38]. At 40 GeV/c the yields of $K^\pm$ in $p + p$ are compared to values extracted from Fig. 132 reported in [10] (open crosses). Lines show results from HSD [36] and UrQMD2.3 [37] calculations as well as from the core-corona model (the latter for the Pb + Pb collision system only [39]). The thin vertical bars indicate the statistical errors, which are mostly not visible. The thick shaded bars indicate the systematic errors.

their maximum already for smaller volumes (number of wounded nucleons) than heavy systems like Pb + Pb. At $158A$ GeV (see right column of Fig. 11) the data points from peripheral Pb + Pb collisions follow nicely the core-corona prediction for the Pb + Pb system. Also the C + C and Si + Si points are consistent with this prediction (for Pb + Pb), although according to Fig. 12 they should be higher even for noncentral collisions of the small C + C and Si + Si systems. However, here the core-corona approach is applied to small system sizes for which the simplification of separating the collision zone into one central cluster and $p + p$ collisions in the periphery might not be valid anymore. Instead, percolation calculations suggest that for such collision systems several clusters of smaller size will be formed [21].

In Fig. 13 we summarize the K^+/π^- ratios for centrality selected Au + Au (Pb + Pb) collisions at different beam energies. The ratios at the different centralities were scaled to the ratios measured in the most central collisions. The observed saturation of strangeness production at SPS energy and above can be understood in the context of statistical models by the approach to a grand-canonical description. Increasing the energy available for particle production no longer changes the multiplicities of strangeness-carrying particles relative to pions [2,3], which means that strangeness becomes fully saturated. Saturation already sets in for rather peripheral collisions. The reduction of relative strangeness production toward even smaller system sizes has been discussed in the framework of the core-corona model in the previous paragraph.

An implementation of this ansatz into the statistical model and a detailed comparison of model calculations to RHIC data can be found in [25]. In order to describe the data satisfactorily it is essential to use a volume dependence which is not just proportional to $\langle N_w \rangle$. The situation is different at low (SIS) energies. Here the K^+/π^- ratio does not saturate and its dependence on the number of wounded nucleons is rather linear. In contrast to the situation at high energies, statistical models can describe the observed centrality dependence at low energy within a canonical ensemble and with a volume proportional to the number of wounded nucleons: $V \propto \langle N_w \rangle$ [20]. Such a behavior would also be expected in a hadronic rescattering scenario as realized in microscopic models [13]. The results obtained at $40A$ GeV are intermediate between those at top SPS and AGS energies. We thus observe a smooth transition between the two scenarios which occurs in the SPS energy region.

D. E_S as a function of system size

The strangeness to entropy ratio or total relative strangeness production described by the Wroblewski factor $\lambda_s = 2\langle s\bar{s} \rangle / \langle u\bar{u} + d\bar{d} \rangle$ can be approximated by the measurable
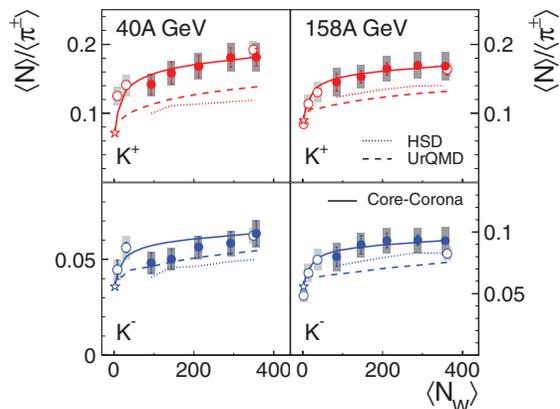
FIG. 11. (Color online) Kaon yields divided by mean number of pions $\langle \pi^{\pm} \rangle = 0.5(\langle \pi^{-} \rangle + \langle \pi^{+} \rangle)$ as a function of centrality. Closed symbols show results from centrality selected Pb + Pb collisions; open symbols show $p + p$ data from NA49 [9,10] as well as C + C, Si + Si (at 158*A* GeV [8]), and central Pb + Pb collisions from [2,3]. The stars denote the values obtained from parametrization "B" in Ref. [38]. Lines show results from HSD [36] and UrQMD2.3 [37] simulations and the core-corona model (the latter for the Pb + Pb collision system only [39]). The thin vertical bars indicate the statistical errors, which are mostly not visible. The thick shaded bars indicate the systematic errors.

quantity $E_S = (\langle N_{\Lambda} \rangle + 2[\langle N_{K^+} \rangle + \langle N_{K^-} \rangle])/(1.5[\langle N_{\pi^+} \rangle + \langle N_{\pi^-} \rangle])$ [2]. The data presented in this paper combined with earlier ones published in [6,8] allow us to study the dependence of E_S on system size for 40*A* GeV and 158*A* GeV beam energy with the 158*A* GeV data covering the whole range of possible sizes. This dependence is shown in Fig. 14 and can now be compared directly to the dependence obtained from statistical model calculations in which for simplicity we assume that $E_S \propto \eta$, with η being the canonical strangeness suppression factor (see, for example, Refs. [18,19]). In statistical models the relative strangeness production depends on the volume of the ensemble. Assuming naively that the volume is proportional to the number of wounded nucleons ([18,19]) yields an increase of relative strangeness production (dashed line in Fig. 14) which is significantly steeper than
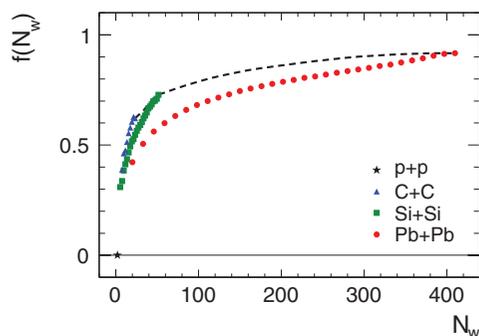

FIG. 12. (Color online) Core fraction obtained in the core-corona model for different collision systems as a function of the number of participating nucleons [39]. The dashed line connects the endpoints of the curves for the different collision systems. $f(\langle N_w \rangle)$ denotes the fraction of those nucleons which undergo more than one collision.
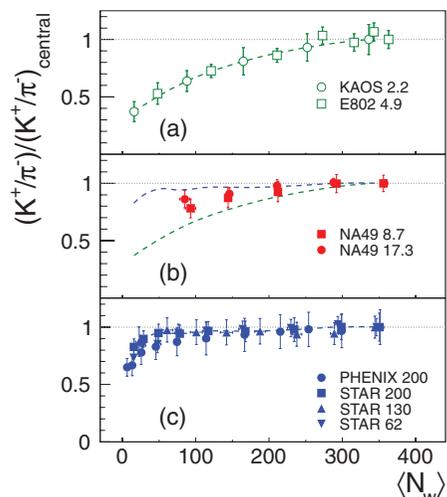

FIG. 13. (Color online) Centrality dependence of the double ratio of the K^+ to π^- multiplicities scaled to the ratios from the corresponding most central measurement minimum-bias Pb + Pb (Au + Au) collisions at SIS [11] and AGS [12,13] energies (a), at SPS energies (b), and at RHIC energies [14,15] (c). The dashed lines in panels (a) and (c) are meant to guide the eye and are also drawn as a reference in panel (b). Only statistical errors are shown.

the increase observed in the data. On the other hand, the smooth rise of E_S with system size and the saturation around 60–100 wounded nucleons is reproduced within experimental errors by a percolation model [21]. In this model the volumes relevant for strangeness production by statistical hadronization are calculated within a percolation ansatz. This yields several smaller clusters in collisions of light nuclei or in peripheral
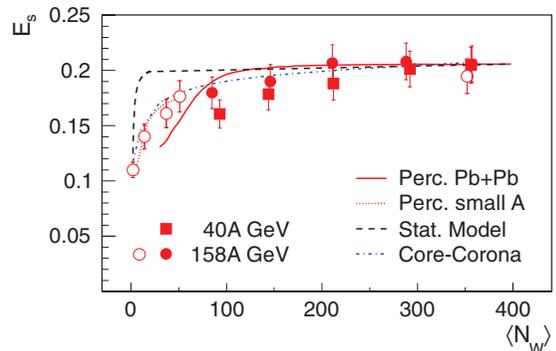

FIG. 14. (Color online) Total relative strangeness approximated by E_S for centrality selected minimum-bias Pb + Pb collisions at 40*A* GeV (squares) and 158*A* GeV (circles) as a function of $\langle N_w \rangle$. The open symbols are from $p + p$ [9,10], C + C, Si + Si [2], S+S [40], and central Pb + Pb [2] at 158*A* GeV. The filled symbols represent the data of centrality selected Pb + Pb collisions at 40*A* GeV and 158*A* GeV (this analysis and [6]). The lines indicate calculations within the statistical model under the assumption of proportionality between ensemble volume and $\langle N_w \rangle$ (dashed), with volumes as derived from percolation calculations for small systems (dotted line) and Pb + Pb collisions (solid line) [21], as well as calculations based on the core-corona ansatz at 158*A* GeV (dash-dotted line). Only statistical errors are shown.

Pb + Pb collisions and a large cluster accompanied by small clusters ($p + p$ interaction like) in the periphery for central Pb + Pb collisions. The latter finding justifies the simplified ansatz used in the core-corona approach, which is shown by the dash-dotted line. The functional dependencies change slightly between light and heavy nuclei (dotted and solid lines in Fig. 14), both describing the data at 158A GeV beam energy well. The Pb + Pb data show a weaker increase at 40A GeV than at 158A GeV.

VI. SUMMARY

The NA49 Collaboration measured the rapidity and transverse mass distributions of kaons and pions in Pb + Pb collisions at different centralities. These data are complemented by results from the small systems C + C and Si + Si. We find that the centrality dependence of kaon and pion production is reproduced by microscopic transport model calculations (HSD and UrQMD2.3) within 20% or better. The mean transverse mass evolves with centrality, as expected for increased stopping and energy deposition. The centrality dependence of the widths of the rapidity distributions in Pb + Pb collisions does not smoothly connect to results from the small systems $p + p$, C + C, and Si + Si. We attribute this behavior to reinteractions of produced particles with spectator remnants, which is possible only in the heavy collision system. In Pb + Pb collisions the K$/\pi$ ratios show a smooth increase with centrality at both beam energies with saturation setting

in around 100–200 (60–100) wounded nucleons for 40A GeV (158A GeV). In particular, at 40A GeV beam energy the ratios measured in C + C and Si + Si collisions tend to be higher than the ratios in peripheral Pb + Pb interactions. The strong rise for small systems can be understood in the framework of statistical models, if the relevant volumes are chosen appropriately. The two models discussed here, the core-corona model and the percolation model, implement this ansatz and can describe the relative strangeness production for 158A GeV (and above). For lower energies disagreements appear.

[1] J. Rafelski and B. Müller, Phys. Rev. Lett. **48**, 1066 (1982).

[2] S. V. Afanasiev *et al.* (NA49 Collaboration), Phys. Rev. C **66**, 054902 (2002).

[3] C. Alt *et al.* (NA49 Collaboration), Phys. Rev. C **77**, 024903 (2008).

[4] A. Andronic, P. Braun-Munzinger, and J. Stachel, Phys. Lett. B **673**, 142 (2009).

[5] C. Amsler *et al.* (Particle Data Group), Phys. Lett. B **667**, 1 (2008).

[6] T. Anticic *et al.* (NA49 Collaboration), Phys. Rev. C **80**, 034906 (2009).

[7] T. Anticic *et al.* (NA49 Collaboration), Phys. Rev. C **83**, 014901 (2011).

[8] C. Alt *et al.* (NA49 Colaboration), Phys. Rev. Lett. **94**, 052301 (2005).

[9] C. Alt *et al.* (NA49 Collaboration), Eur. Phys. J. C **45**, 343 (2006).

[10] T. Anticic *et al.* (NA49 Collaboration), Eur. Phys. J. C **68**, 1 (2010).

[11] A. Förster *et al.*, J. Phys. G **31**, S693 (2005).

[12] L. Ahle *et al.*, Phys. Rev. C **60**, 044904 (1999).

[13] F. Wang, H. Liu, H. Sorge, N. Xu, and J. Yang, Phys. Rev. C **61**, 064904 (2000).

[14] S. S. Adler *et al.* (Phenix Collaboration), Phys. Rev. C **69**, 034909 (2004).

[15] B. I. Abelev *et al.* (STAR Collaboration), Phys. Rev. C **79**, 034909 (2009).

[16] F. Becattini, M. Gazdzicki, A. Keranen, J. Manninen, and R. Stock, Phys. Rev. C **69**, 024905 (2004).

[17] F. Becattini, J. Manninen, and M. Gaździcki, Phys. Rev. C **73**, 044905 (2006).

[18] J. Rafelski and M. Danos, Phys. Lett. B **97**, 279 (1980).

[19] A. Tounsi and K. Redlich, J. Phys. G **28**, 2095 (2002).

[20] J. Cleymans, H. Oeschler, and K. Redlich, Phys. Rev. C **59**, 1663 (1999).

[21] C. Höhne, F. Pühlhofer, and R. Stock, Phys. Lett. B **640**, 96 (2006).

[22] K. Werner, Phys. Rev. Lett. **98**, 152301 (2007).

[23] P. Bozek, Acta Phys. Pol. B **36**, 3071 (2005).

[24] R. J. Glauber, Phys. Rev. **100**, 242 (1955).

[25] F. Becattini and J. Manninen, Phys. Lett. B **673**, 19 (2009).

[26] J. Aichelin and K. Werner, Phys. Rev. C **79**, 064907 (2009).

[27] S. Afanasiev *et al.*, Nucl. Instrum. Methods A **430**, 210 (1999).

[28] A. Laszlo, Ph.D. thesis, KFKI Research Institute for Particle and Nuclear Physics, Budapest, CERN EDMS ID 942284, 2007.

[29] K. Werner, Phys. Rep. **232**, 87 (1993).

[30] C. Alt *et al.* (NA49 Collaboration) Phys. Rev. C **77**, 034906 (2008). Details can be obtained from [https://edms.cern.ch/file/885329/1/vetocal2.pdf].

[31] B. Lungwitz, Diploma thesis, Goethe-Universität Frankfurt, CERN EDMS ID 1159529, 2004.

[32] T. Anticic *et al.* (NA49 Collaboration), Phys. Rev. C **83**, 014901 (2011).

[33] R. Brun *et al.*, GEANT User Guide, CERN/DD/EE84-1, 1986.

[34] P. Dinkelaker, Ph.D. thesis, Goethe-Universität Frankfurt, CERN EDMS ID 1142684/1, 2009.

[35] M. Kliemant Diploma thesis, Goethe-Universität Frankfurt, CERN EDMS ID 1159527/1, 2005.

[36] W. Ehehalt and W. Cassing, Nucl. Phys. A **602**, 449 (1996); W. Cassing and E. L. Bratkovskaya, Phys. Rep. **308**, 65 (1999).

[37] H. Petersen, M. Bleicher, S. A. Bass, and H. Stöcker, arXiv:0805.0567 [hep-ph]; M. Mitrovski (private communication).

[38] A. M. Rossi *et al.*, Nucl. Phys. B **84**, 269 (1975).

[39] C. Blume, J. Phys. Conf. Ser. **230**, 012003 (2010).

[40] T. Alber *et al.*, Z. Phys. C **64**, 195 (1994).